Cover Page

Universiteit Leiden

Leiden University Repository

The handle http://hdl.handle.net/1887/28962 holds various files of this Leiden University dissertation

Author: Sande, Jesse van de
Title: Dawn of the red and dead stellar kinematics of massive quiescent galaxies out to z = 2
Issue Date: 2014-10-01

2 The stellar velocity dispersion of a compact massive galaxy at $z = 1.80$ using X-Shooter: confirmation of the evolution in the mass-size and mass-dispersion relations

Abstract

Recent photometric studies have shown that early-type galaxies at fixed stellar mass were smaller and denser at earlier times. In this chapter we assess that finding by deriving the dynamical mass of such a compact quiescent galaxy at z=1.8. We have obtained a high-quality spectrum with full UV-NIR wavelength coverage of galaxy NMBS-C7447 using X-Shooter on the Very Large Telescope. We determined a velocity dispersion of 294±51 km s^{-1}. Given this velocity dispersion and the effective radius of 1.64±0.15 kpc (as determined from *Hubble Space Telescope* Wide Field Camera 3 F160W observations) we derive a dynamical mass of 1.7±0.5 $\times$ $10^{11} M_{\odot}$. Comparison of the full spectrum with stellar population synthesis models indicates that NMBS-C774 has a relatively young stellar population (0.40 Gyr) with little or no star formation and a stellar mass of $M_{\star} \sim 1.5 \times 10^{11} M_{\odot}$. The dynamical and photometric stellar mass are in good agreement. Thus, our study supports the conclusion that the mass densities of quiescent galaxies were indeed higher at earlier times, and this earlier result is not caused by systematic measurement errors. By combining available spectroscopic measurements at different redshifts, we find that the velocity dispersion at fixed dynamical mass was a factor of ~1.8 higher at z=1.8 compared to z=0. Finally, we show that the apparent discrepancies between the few available velocity dispersion measurements at $z > 1.5$ are consistent with the intrinsic scatter of the mass-size relation.

Jesse van de Sande, Mariska Kriek, Marijn Franx, Pieter G. van Dokkum,
Rachel Bezanson, Katherine E. Whitaker, Gabriel Brammer, Ivo Labbé,
Paul J. Groot, and Lex Kaper
The Astrophysical Journal Letters, **736**, L9:L16, (2011)

2.1 Introduction

In hierarchical structure formation models, the most massive early-type galaxies are assembled last (e.g., Springel et al., 2005). This simple picture seems difficult to reconcile with recent studies showing that the first massive, quiescent galaxies were already in place when the universe was only $\sim$3 Gyr old (e.g., Labbé et al. 2005; Kriek et al. 2006; Williams et al. 2009). The recent discovery that these high-redshift galaxies still grow significantly in size (e.g., Daddi et al. 2005; Trujillo et al. 2006; van Dokkum et al. 2008), and mass (van Dokkum et al., 2010) solves this apparent conflict. The observed compact high-redshift galaxies may simply be the cores of local massive early-type galaxies, which grow inside-out by accreting (smaller) galaxies (e.g., Naab et al. 2009; Bezanson et al. 2009; van der Wel et al. 2009), and thus assemble a significant part of their mass at later times (see also Oser et al. 2010).

However, the results may be interpreted incorrectly due to systematic uncertainties. First, sizes may have been underestimated, as low-surface brightness components might have been missed (Mancini et al., 2010). Nonetheless, recent work using stacking techniques (e.g., van der Wel et al. 2008; Cassata et al. 2010; van Dokkum et al. 2010), and ultra-deep *Hubble Space Telescope* Wide Field Camera 3 (*HST*-WFC3) data (e.g., Szomoru et al., 2010), demonstrated that radial profiles can now be measured with high accuracy extending to large radii. Second, the stellar mass estimates suffer from uncertainties in stellar population synthesis (SPS) models, the paucity of spectroscopic redshifts, and furthermore rely on assumptions regarding the initial mass function (IMF) and metallicity (e.g., Conroy et al., 2009). Direct kinematic mass measurements, which are not affected by these uncertainties, are needed to confirm the high stellar masses and densities of these galaxies.

Kinematic measurements have only recently become possible for high-redshift galaxies (e.g., Cenarro & Trujillo, 2009). Using optical spectroscopy, Newman et al. (2010) have explored the epoch up to $z \sim 1.5$. With near-infrared (NIR) spectroscopy these studies have been pushed to even higher redshift. Using a $\sim$29 hr spectrum of an ultra-compact galaxy at $z = 2.2$ obtained with Gemini Near-IR Spectrograph (Kriek et al., 2009), van Dokkum et al. (2009b) found a high, though uncertain velocity dispersion of $\sigma = 510^{+165}_{-95}$km s^{-1}. Onodera et al. (2010) used the MOIRCS on the Subaru telescope to observe the rest-frame optical spectrum of a less-compact, passive, ultra-massive galaxy at $z = 1.82$, but the low spectral resolution only allowed the determination of an upper limit to the velocity dispersion of $\sigma < 326$ km s^{-1}. With the lack of high-quality dynamical data at $z > 1.5$ there still is no general consensus on the matter of compact quiescent galaxies.

Here we present the first high signal-to-noise ratio (S/N), high-resolution, UV-NIR spectrum of a $z = 1.80$ galaxy observed with X-Shooter (D'Odorico et al., 2006) on the Very Large Telescope (VLT). Throughout the chapter we assume a ΛCDM cosmology with $\Omega_{\rm m}$=0.3, $\Omega_\Lambda = 0.7$, and $H_0 = 70$ km s^{-1} Mpc^{-1}. All broadband data are given in the AB-based photometric system.

2.2 Observations and reduction

The target is selected from the NEWFIRM Medium-Band Survey (NMBS; van Dokkum et al. 2009; Whitaker et al. 2011). This target, NMBS-C7447 ($\alpha = 10^{\rm h}00^{\rm m}06.955^{\rm s}$, $\delta =$

$02^{\mathrm{d}}17^{\mathrm{m}}33.603^{\mathrm{s}}$), was selected as it is among the brightest ($K_{\mathrm{tot}} = 19.64$), quiescent galaxies in the COSMOS field. As the galaxy was selected for its apparent magnitude, it is probably younger than the typical quiescent galaxy at its redshift (Whitaker et al., 2010). A radio counterpart was detected, with $L = 9.789 \times 10^{24}$ W m^{-2}Hz^{-1} (Schinnerer et al., 2010).

The galaxy was observed for 2 hr with X-Shooter on the VLT/UT2 on 2010 January 21st, with clear sky conditions and an average seeing of $0\farcs8$ X-Shooter consists of three arms: UVB, VIS, and NIR, resulting in a simultaneous wavelength coverage from 3000 Å to 24800 Å. The NIR part of the spectrum is the most interesting, as it covers many of he strong rest-frame optical stellar absorption features. A $0\farcs9$ slit was used ($R = 5600$ at 1.5 μm). The 2 hr of observing time were split in 8 exposures of 15 minutes each with an ABA'B' on-source dither pattern. A telluric standard of type B9V was observed for calibration purposes.

We use a similar procedure to reduce cross-dispersed NIR spectra as in Kriek et al. (2008); details will be given in Chapter 3. The resulting two-dimensional spectrum was visually inspected for emission lines, but none were found. A one-dimensional spectrum was extracted by adding all lines (along wavelength direction), with flux greater than 0.1 times the flux in the central row, using optimal weighting. Our results do not change if we take a different flux limit for extraction. This high-resolution spectrum has a S/N 10.4 Å$^{-}1$ in rest frame in H. A low-resolution spectrum was constructed by binning the two-dimensional spectrum in wavelength direction. Using a bi-weight mean, 20 good pixels, i.e., not affected by skylines or strong atmospheric absorption, were combined. The one-dimensional spectrum was extracted from this binned two-dimensional spectrum in a similar fashion as the high-resolution spectrum (see Figure 2.1).

For the UVB and VIS arm, the two-dimensional spectra were reduced using the ESO pipeline (1.2.2, Goldoni et al. 2006). Correction for the atmospheric absorption and one-dimensional extraction were performed in a similar way as the NIR arm as described above.

2.3 Stellar population and structural properties

2.3.1 Stellar population properties

We estimate the redshift, age, dust content, star formation timescale, metallicity, stellar mass, star formation rate (SFR), and their confidence intervals by fitting the low-resolution spectrum in combination with the broadband photometry with SPS models. We use the fitting code FAST (Kriek et al., 2009b) in combination with the stellar templates by Bruzual & Charlot (2003) (hereafter BC03; see Kriek et al. 2010). An exponentially declining star formation history with timescale τ is assumed, together with a Chabrier (2003) IMF, and the Calzetti et al. (2000) reddening law. We scale the mass by the ratio between the total F160W flux in the best-fit GALFIT model (see Section 2.3.2), and the total H band flux in the NMBS catalog. The galaxy spectrum is best-fit with a stellar mass of $M_{\star} = 1.5 \times 10^{11}$ $M_{\odot}$, $\tau = 0.03$ Gyr, an age of 0.40 Gyr, SFR of 0.002 $M_{\odot}$ yr^{-1}, $A_V = 0.20$, solar metallicity, and a redshift of 1.800 (see Figure 2.1). In order to account for systematic uncertainties (e.g., Conroy et al., 2009), we will assume an error of ~0.2 dex in $M_{\star}$. The galaxy is not detected at 24 μm, leading to a 3 σ (~20 μJy) upper limit to the dust-enshrouded SFR of $< 15 M_{\odot}$ yr^{-1}.

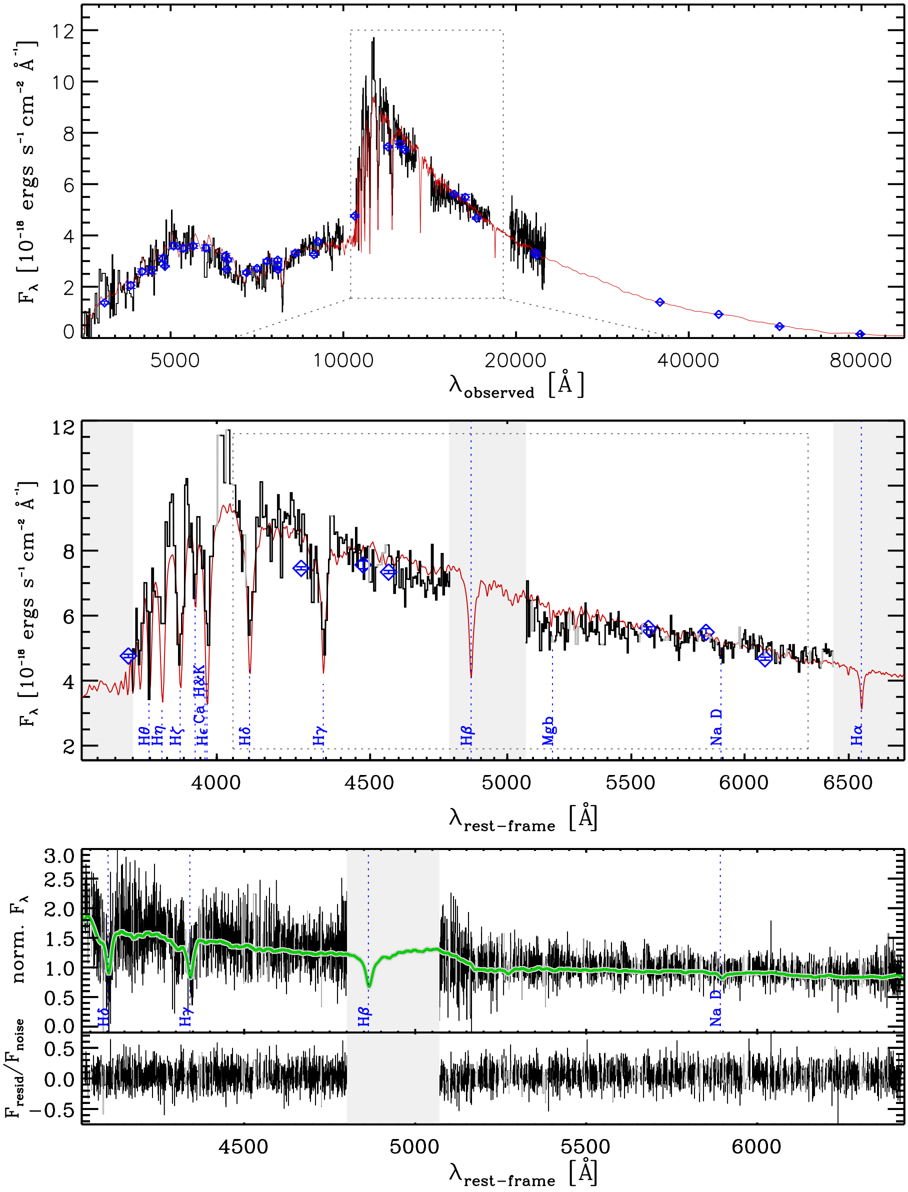

Figure 2.1: X-Shooter spectrum of NMBS-C7447 and the best-fit stellar population model (red line). Top panel: broad and medium-band data (blue diamonds) in combination with low-resolution spectrum (10 Å bin^{-1}). The entire wavelength range from UV (0.35μm) to NIR(2.3μm) is covered in 2 hr integration time with unprecedented quality. The galaxy is best fit with a young stellar population (0.40 Gyr, $\tau = 0.03$Gyr) with little star formation (0.002 $M_\odot$ yr^{-1}) and a stellar mass of $M_\star \sim 1.5 \times 10^{11}$ $M_\odot$. Middle panel: zoom in on the rest-frame optical part of the spectrum. Gray areas indicate regions of strong skylines or atmospheric absorption. Most prominent stellar absorption features are indicated with blue dashed line. Bottom two panels: high resolution spectrum (0.5 Å bin) of the observed features used to determine the stellar velocity dispersion. The green line is the best fit for the velocity dispersion with 4020 Å$< \lambda_{\mathrm{rest-frame}} <$6400 Å using the pPFX code (Cappellari & Emsellem, 2004). The resulting stellar velocity dispersion is σ_* = 294±51 km s^{-1}. The residual from the best fit divided by the noise is shown in the bottom panel.

2.3.2 Size measurement

We obtained *HST*-WFC3 F160W imaging of NMBS-C7447 in 2010 October (*HST*-GO-12167.1, see Figure 2.2) to measure its size by fitting a Sérsic radial surface brightness profile (Sérsic, 1968), using the two-dimensional fitting program GALFIT (version 3.0.2; Peng et al. 2010). The blue object to the north was masked in the fit, as it is unclear whether it is part of the galaxy. All parameters, including the sky, were left free for GALFIT to determine, and three nearby field stars were used for the point-spread-function (PSF) convolution.

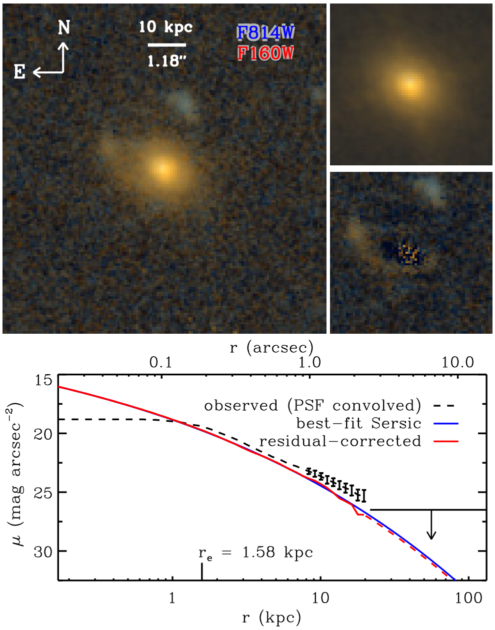

Figure 2.2: Left panel: *HST* color image of NMBS-C7296, consisting of ACS-F775W (blue) and WFC3-F160W (red). Top right panel: best-fit Sérsic model convolved with the PSF from GALFIT. The best-fit effective radius is $r_e = 1.64 \pm 0.15$ kpc and $n = 5.3 \pm 0.4$. Bottom right panel: remaining residual after subtracting the model from the observed image divided by the noise. Bottom panel: observed radial profile of NMBS-C7447, in comparison with the best-fit Sérsic profile and the residual-corrected profile, as described by Szomoru et al. (2010).

In WFC3 F160W we find a mean circularized effective radius of 1.64±0.15 kpc, a mean Sérsic n-parameter of 5.3±0.4, and an axis ratio $b/a = 0.71 \pm 0.01$. The uncertainties reflect both sky noise and PSF uncertainties, which were simulated using different field stars. We find the same effective radius if we use the residual-corrected method as described by Szomoru et al. (2010). We also analyzed an ACS I-band image from the COSMOS survey (Scoville et al. 2007; Koekemoer et al. 2007). The target has an effective radius of r_e=1.95±0.20 kpc with n=5.6±0.4, using the same PSF stars as for WFC3. An arclike feature is present in the residual image, to the southeast of the object (within $1\farcs5$, and ~3 mag fainter than the main target). This may indicate that the galaxy is undergoing a tidal interaction (see also van Dokkum & Brammer 2010). In what follows, we will use the mean effective radius obtained with WFC3 F160W(H), as this band coincides with rest-frame optical for our z ~1.8 galaxy.

2.3.3 Velocity dispersion

We use our high-resolution spectrum, and the Penalized Pixel-Fitting method (pPXF) developed by Cappellari & Emsellem (2004) to measure an accurate stellar velocity dispersion for NMBS-C7447. Four different templates were used: the best-fit BC03 SPS model (σ=85 kms^{-1}), Munari synthetic stellar library (Munari et al. 2005, σ=6.4 kms^{-1}), Indo US Library (Valdes et al. 2004, σ=38.2 kms^{-1}), and the Miles library (Sánchez-Blázquez et al. 2006, σ=71.9 kms^{-1}). Except for the best-fit SPS model, pPXF was used to construct an optimal template in combination with a 30th-order Legendre Polynomial. The fit was restricted to 4020 Å$<\lambda<$6400 Å, in order to exclude the Balmer break region and the noisier K-band. Figure 2.1 (bottom panels) shows the high-resolution spectrum with the best-fit velocity dispersion model from pPXF in red using the best-fit SPS model.

After correcting for instrumental resolution (σ=23 km s^{-1}) and the spectral resolution of the templates, we find a best-fitting velocity dispersion of $\sigma_{\rm obs}$=284±51 km s^{-1}. The error was determined in the following way. We subtracted the best-fit template from the spectrum. This residual was randomly rearranged in wavelength space and added to best-fit template. We determined the velocity dispersion of 1000 simulated spectra. Our quoted error is the standard deviation of the resulting distribution of σ. When we include the Balmer break region in the fit, the formal error decreases, but the derived dispersion becomes very dependent on the chosen stellar template. Fitting the full-wavelength range gives a consistent result of σ_*= 328± 35 km, but we prefer to use the method above as it is the most robust.

The stellar velocity dispersion is corrected to match the average dispersion as would be observed within an aperture radius of r_e. Our approach is similar to Cappellari et al. (2006), but taken into account the effects of a non-circular aperture, seeing, and optimized extraction. The aperture correction is only 3.5%, resulting in a velocity dispersion of σ_e=294±51 kms^{-1} (see Chapter 3).

The dynamical mass is derived using

$$M_{\rm dyn} = \frac{\beta(n)\ \sigma_\star^2\ r_e}{G} \tag{2.1}$$

where $\beta(n)$ is an analytic expression as a function of the Sérsic index, as described by Cappellari et al. (2006). Using $n = 5.27$, we find $\beta = 5.16$, and a dynamical mass for NMBS-C7447 of 1.7±0.5×10^{11} $M_\odot$.

2.4 Evolution

In this section we compare our results to low- and high-redshift measurements, and discuss the implications for the evolution of quiescent galaxies. Figure 2.3 shows our results, together with other kinematical studies at $z > 1$, and galaxies from the Sloan Digital Sky Survey (SDSS) at $0.05 < z < 0.07$ (York et al., 2000). The SDSS structural parameters are from Franx et al. (2008), though we only select non-starforming galaxies (i.e., specific SFR $< 0.3/t_H$, see Williams et al. 2009). For all galaxies, velocity dispersions were corrected as described in Section 2.3.3, and stellar masses were converted to a Chabrier (2003) IMF. All dynamical masses were derived using Equation 2.1.

Many high-redshift studies rely on photometric stellar masses, which suffer from large uncertainties (e.g., Conroy et al., 2009). Here, we test these stellar masses by comparing them to our dynamical measurements (Figure 2.3(a)). The dynamical and stellar mass for NMBS-C7447 are in agreement, and consistent with the relation for low-redshift galaxies. Given this good agreement, we should be able to predict the velocity dispersion from the size and stellar mass measurements.

We assume a constant ratio of $M_{\rm dyn}/M_\star = 1.68$, which is the average ratio for the SDSS sample, to account for dark matter and systematic uncertainties in the stellar mass estimate.

We show the results in Figure 2.3(b). The predicted velocity dispersions of NMBS-C7447, and the other $z > 1.5$ galaxies are consistent with the observed velocity dispersions. This illustrates the robustness of our size and mass measurements.

In Figure 2.3(c) we show the velocity dispersion vs. the effective radius. Similar to what has been found for other high-redshift studies, NMBS-C7447 has a clear offset from the low-redshift galaxy population. Its velocity dispersion is higher compared to $z \sim 0.06$ galaxies with similar radii. The mass size relation is shown in Figure 2.3(d) and (e). The effective radius of our galaxy is smaller compared to local galaxies at similar masses, confirming other studies at high redshift. From Figure 2.3(f), where we show the dynamical mass vs. the observed velocity dispersion, we find that NMBS-C7447 has a higher velocity dispersion than similar-mass SDSS galaxies, in agreement with other studies of high-redshift compact galaxies.

We parameterize the mass-size relation by (Shen et al. 2003,van der Wel et al. 2008):

$$r_e = r_c \left(\frac{M_{\text{dyn}}}{10^{11} M_\odot} \right)^b . \tag{2.2}$$

Using a least-squares fit to the low-redshift galaxy sample, we find $r_c = 3.32$kpc, and $b = 0.50$. When comparing NMBS-C7447 to local galaxies at fixed dynamical mass, we find that the effective radius is a factor ~2.5 smaller. We use a similar approach for the velocity dispersion as a function of dynamical mass (Figure 2.3(f)):

$$\sigma_\star = \sigma_c \left(\frac{M_{\text{dyn}}}{10^{11} M_\odot} \right)^b , \tag{2.3}$$

with $\sigma_c = 145\text{kms}^{-1}$, and $b = 0.26$. NMBS-C7447 has a higher velocity dispersion by a factor ~ 1.8 compared to the low-redshift relation.

Figure 2.4 shows the evolution of the sizes and velocity dispersions of the galaxies, normalized to a standard dynamical mass using Equations 2.2 and 2.3. We add the sample by van der Wel et al. (2008) for a more complete redshift coverage, with stellar masses derived from the FIRES (Förster Schreiber et al., 2006) and FIREWORKS catalog (Wuyts et al., 2008). We use a simple power law fit $r_e \propto (1+z)^\alpha$ for galaxies with $M_{\text{dyn}} > 3 \times 10^{10} M_\odot$ and find $\alpha = -0.98 \pm 0.09$. This is in agreement with van der Wel et al. (2008), but slightly higher than Newman et al. (2010). Our results imply a growth in size at fixed mass by a factor of ~ 2.5 from $z \sim 1.8$ to the present day. When assuming a similar power law for the velocity dispersion ($\sigma_\star \propto (1+z)^{0.51 \pm 0.07}$), we find a decrease in velocity dispersion by a factor of ~ 1.5 from $z \sim 1.8$ to the present day at fixed mass.

Figures 2.4a and b show that the scatter in the relation in the normalized size and velocity dispersion is large at fixed redshift. At $z > 1.5$, three galaxies have been observed with a range in normalized dispersions of a factor of ~ 2.5. This may lead to the conclusion that the measurements have large unidentified errors and cannot be trusted yet. On the other hand, intrinsic scatter in the galaxy properties may cause this rather large observed scatter. We can test this directly by using the deviations of the galaxies in the mass-size relation.

If the scatter is due to variations in the intrinsic properties, we expect that the deviations of the galaxies in the mass-size relation correlate with the deviations of the galaxies in the mass-dispersion relation. If the scatter is observational, there is no expected correlation. In Figure 2.4(c), we compare the deviation from the $M_\star - r_e$ relation to the deviations in the

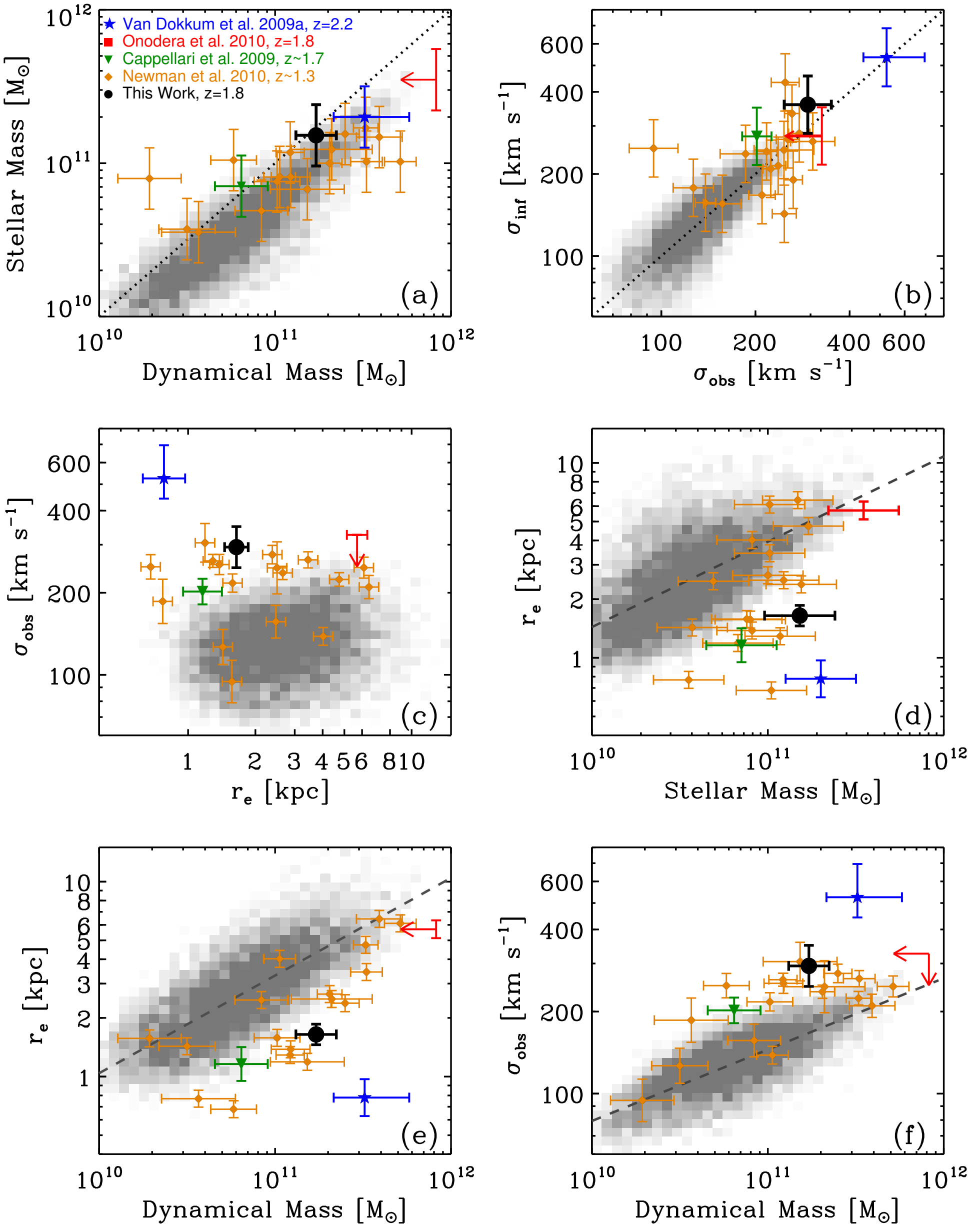

Figure 2.3: Comparison of NMBS-C7447 (black filled circle) with other high-redshift studies (see legend in panel (a)) and quiescent low-redshift galaxies in the SDSS (grey scale). (a) Dynamical vs. stellar mass. The dynamical and stellar masses are consistent, but differ by a constant factor, which can be due to dark matter and systematic effects on the stellar mass estimates. (b) Measured vs. inferred velocity dispersions (as inferred from the stellar mass and size). The observed dispersion agrees well with inferred dispersion, which implies that the stellar mass and size measurements are robust. (c) σ_{obs} vs. r_{e}. NMBS-C7447 is offset from the low-redshift galaxies plane. (d and e) r_{e} vs. stellar and dynamical mass. The dashed gray lines are the best-fit low-redshift relations (Equation 2.2). NMBS-C7447 is a factor of $\sim$2.5 smaller than low-redshift galaxies at fixed mass. (f) σ_{obs} vs. dynamical mass. The velocity dispersion of NMBS-C7447 is a factor $\sim$1.8 higher than similar-mass low-redshift galaxies.

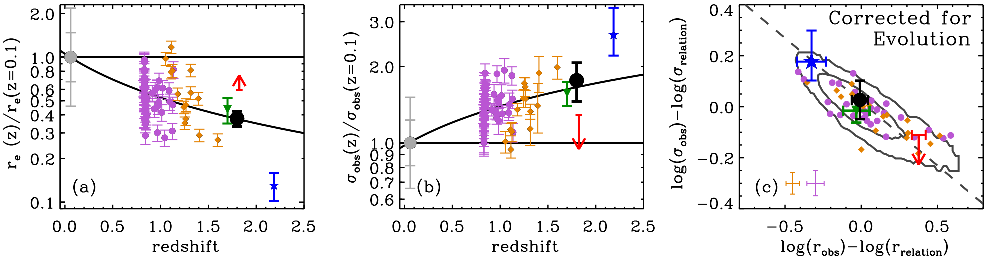

Figure 2.4: Evolution in effective radius and velocity dispersion at fixed dynamical mass, thus corrected for the $M_{\rm dyn}-r_e$ and $M_{\rm dyn}-\sigma_{\rm obs}$ relations from Figure 2.3(e) and 2.3f. We only select galaxies with $M_{\rm dyn} > 3\times10^{10}M_{\odot}$. Symbols are as described in Figure 2.3, with the addition of data from van der Wel et al. 2008 (purple circles). The gray filled circle at $z\sim 0.06$ shows the median from the SDSS, with the error indicating the 1σ and 2σ scatter. The solid lines show a simple best fit to the data of $(1+z)^{-0.98\pm0.09}$ for the evolution in effective radius, and $(1+z)^{0.51\pm0.07}$ for the velocity dispersion. (c) Scatter in the $M_\star - r_e$ relation vs. the scatter in the $M_{\rm dyn}-\sigma_{\rm obs}$ relations, together with the 1σ and 2σ contours of the SDSS galaxies, all corrected for evolution. The discrepancy between the different measurements is expected based on the intrinsic scatter in the low-redshift relations.

$M_{\rm dyn}-\sigma_{\rm obs}$ relation. The deviation of the $M_\star - r_e$ and $M_{\rm dyn}-\sigma_{\rm obs}$ relations were derived using the evolution of these relations at fixed mass as shown in Figures 2.4(a) and (b).

We can predict, using the virial theorem, how the points would lie if the scatter is intrinsic, i.e., due to variations in the galaxy structure. This line is shown in Figure 2.4(c), and we see that the galaxies lie very close to this line. In addition, we show the area which is covered by the SDSS galaxies in the same diagram (1σ and 2σ contours). Almost all data points lie within these contours. Hence we conclude that the scatter is mostly *intrinsic*, and not observational. A direct measure of the average offset of the sizes and dispersions can be obtained by increasing the number of observed galaxies to about 30, which would reduce the error by a factor of ~ 3. Alternatively, the average mass-size relation can be used to determine the average offset at $z = 1.5-2$. Thus we conclude that the difference between our results and those by van Dokkum et al. (2009b) and Onodera et al. (2010) are due to intrinsic scatter in galaxy properties.

2.5 Conclusions

In this chapter we have presented the first high-S/N, high-resolution, spectrum of a compact massive quiescent galaxy at $z = 1.80$ observed with X-Shooter. Using this spectrum we have determined the stellar mass and velocity dispersion: $M_\star \sim 1.5\times10^{11}M_{\odot}$, $\sigma_{\rm obs} = 294\pm 51{\rm km\ s^{-1}}$. From *HST*-WFC3 imaging we find that $r_e = 1.64\pm0.15{\rm kpc}$. The stellar mass and dynamical mass agree well ($M_{\rm dyn} = 1.7\pm0.5\times10^{11}M_{\odot}$), and are consistent with the local SDSS relation. Our results suggest that stellar masses at high redshift are robust, and thus supports the claim that massive, quiescent galaxies with high stellar mass densities at $z\sim 2$ exist.

When comparing this galaxy to low-redshift early-type galaxies, we find that it is structurally different. At fixed dynamical mass, NMBS-C7447 is smaller by a factor ~ 2.5, and has a higher velocity dispersion by a factor of ~ 1.8.

Despite the high accuracy of our derived stellar parameters, our study is still limited to a single high-redshift galaxy, and it brings the total number of stellar kinematic measurements for individual galaxies at $z > 1.5$ to three. We have shown that the differences between the three measurements can be explained by the scatter in the mass-size relation. A larger sample of compact massive quiescent galaxies at high redshift is needed to accurately measure the structural evolution of these galaxies with cosmic time.

Acknowledgements

We thank Johan Fynbo and Joanna Holt on the reduction of the UVB and VIS X-Shooter data, and the NMBS team for their contribution. This research was supported by grants from the Netherlands Foundation for Research (NWO), the Leids Kerkhoven-Bosscha Fonds. Support for program HST-GO-12167.1 was provided by NASA through a grant from the Space Telescope Science Institute.

References

Bezanson, R., van Dokkum, P. G., Tal, T., Marchesini, D., Kriek, M., Franx, M., & Coppi, P. 2009, ApJ, 697, 1290
Bruzual, G., & Charlot, S. 2003, MNRAS, 344, 1000
Calzetti, D., Armus, L., Bohlin, R. C., Kinney, A. L., Koornneef, J., & Storchi-Bergmann, T. 2000, ApJ, 533, 682
Cappellari, M., & Emsellem, E. 2004, PASP, 116, 138
Cappellari, M., et al. 2006, MNRAS, 366, 1126
Cappellari, M., et al. 2009, ApJ, 704, L34
Cassata, P., et al. 2010, ApJ, 714, L79
Cenarro, A. J., & Trujillo, I. 2009, ApJ, 696, L43
Chabrier, G. 2003, PASP, 115, 763
Conroy, C., Gunn, J. E., & White, M. 2009, ApJ, 699, 486
Daddi, E., et al. 2005, ApJ, 626, 680
D'Odorico, S., et al. 2006, Proc. SPIE, 6269,
Förster Schreiber, N. M., et al. 2006, AJ, 131, 1891
Franx, M., van Dokkum, P. G., Schreiber, N. M. F., Wuyts, S., Labbé, I., & Toft, S. 2008, ApJ, 688, 770
Goldoni, P., et al. 2006, Proc. SPIE, 6269,
Koekemoer, A. M., et al. 2007, ApJS, 172, 196
Kriek, M., et al. 2006, ApJ, 649, L71
Kriek, M., et al. 2008, ApJ, 677, 219
Kriek, M., van Dokkum, P. G., Labbé, I., Franx, M., Illingworth, G. D., Marchesini, D., & Quadri, R. F. 2009a, ApJ, 700, 221
Kriek, M., van Dokkum, P. G., Franx, M., Illingworth, G. D., & Magee, D. K. 2009b, ApJ, 705, L71
Kriek, M., et al. 2010, ApJ, 722, L64
Labbé, I., et al. 2005, ApJ, 624, L81
Mancini, C., et al. 2010, MNRAS, 401, 933
Munari, U., Sordo, R., Castelli, F., & Zwitter, T. 2005, A&A, 442, 1127
Naab, T., Johansson, P. H., & Ostriker, J. P. 2009, ApJ, 699, L178
Newman, A. B., Ellis, R. S., Treu, T., & Bundy, K. 2010, ApJ, 717, L103
Onodera, M., et al. 2010, ApJ, 715, L6
Oser, L., Ostriker, J. P., Naab, T., Johansson, P. H., & Burkert, A. 2010, ApJ, 725, 23
Peng, C. Y., Ho, L. C., Impey, C. D., & Rix, H.-W. 2010, AJ, 139, 2097
Sánchez-Blázquez, P., et al. 2006, MNRAS, 371, 703
Schinnerer, E., et al. 2010, ApJS, 188, 384
Scoville, N., et al. 2007, ApJS, 172, 1
Sérsic, J. L. 1968, Cordoba, Argentina: Observatorio Astronomico, 1968,
Shen, S., Mo, H. J., White, S. D. M., Blanton, M. R., Kauffmann, G., Voges, W., Brinkmann, J., & Csabai, I. 2003, MNRAS, 343, 978
Springel, V., et al. 2005, Nature, 435, 629
Szomoru, D., et al. 2010, ApJ, 714, L244
Trujillo, I., et al. 2006, MNRAS, 373, L36
Valdes, F., Gupta, R., Rose, J. A., Singh, H. P., & Bell, D. J. 2004, ApJS, 152, 251
van Dokkum, P. G., et al. 2008, ApJ, 677, L5
van Dokkum, P. G., et al. 2009a, PASP, 121, 2
van Dokkum, P. G., Kriek, M., & Franx, M. 2009b, Nature, 460, 717
van Dokkum, P. G., et al. 2010, ApJ, 709, 1018
van Dokkum, P. G., & Brammer, G. 2010, ApJ, 718, L73
van der Wel, A., Holden, B. P., Zirm, A. W., Franx, M., Rettura, A., Illingworth, G. D., & Ford, H. C. 2008, ApJ, 688, 48
van der Wel, A., Bell, E. F., van den Bosch, F. C., Gallazzi, A., & Rix, H.-W. 2009, ApJ, 698, 1232
Whitaker, K. E., et al. 2010, ApJ, 719, 1715
Whitaker, K. E., et al. 2011, in press, arXiv:1105.4609
Williams, R. J., Quadri, R. F., Franx, M., van Dokkum, P., & Labbé, I. 2009, ApJ, 691, 1879
Wuyts, S., Labbé, I., Schreiber, N. M. F., Franx, M., Rudnick, G., Brammer, G. B., & van Dokkum, P. G. 2008, ApJ, 682, 985
York, D. G., et al. 2000, AJ, 120, 1579